ACCEPTED MANUSCRIPT

In silico modeling of selected phloroglucinol derivatives from *Rhodomyrtus tomentosa*: Mechanistic insights into their potential against cervical cancer

HUNG DUC NGUYEN*

Thai Nguyen University of Education, 24000 Thai Nguyen, VietNam.

Abstract: Cervical cancer remains a major cause of morbidity and mortality worldwide, driven primarily by persistent infection with high-risk HPV types. Natural phloroglucinol derivatives from *Rhodomyrtus tomentosa* have demonstrated anti-cervical cancer potential; however, their apoptosis-related mechanisms remain insufficiently characterized. In this work, selected phloroglucinol derivatives were evaluated as potential inhibitors of the anti-apoptotic Bcl-2 protein (PDB: 6GL8) through an integrated in silico pipeline that combines molecular docking, 100 ns molecular dynamics simulations, MM/GBSA binding free-energy estimation, ADMET profiling, and DFT-based electronic analysis. Docking prioritized CPD1 as the most favorable ligand (-37.36 kJ/mol), outperforming Belzutifan (-25.73 kJ/mol) and engaging the conserved binding pocket. MD trajectories supported stable complex formation across 100 ns. MM/GBSA further indicated stronger binding for CPD1 (ΔTOTAL = -138.78 ± 15.4 kJ/mol) relative to Belzutifan (-63.72 ± 14.31 kJ/mol), primarily due to more favorable gas-phase interactions, while maintaining a comparable solvation term. ADMET predictions suggested similar solubility but higher intestinal absorption for CPD1, alongside a hERG II alert that warrants cardiotoxicity-oriented optimization. DFT descriptors were consistent with the enhanced electrophilic character of CPD1. Collectively, CPD1 is computationally prioritized as a candidate scaffold for follow-up experimental validation and structure-guided refinement.

Keywords: anti-apoptosis; *Bcl-2*; cervical cancer; molecular modeling; phloroglucinol derivatives; *Rhodomyrtus tomentosa*.

INTRODUCTION

Cervical cancer is indeed the fourth most common cancer in women globally, causing significant mortality, especially in low-and-middle-income countries, with over 660,000 cases and 350,000 deaths reported in 2022.[1] A persistent infection

---

with certain types of high-risk Human Papillomavirus (HPV) is the primary cause of virtually all cervical cancers, though most HPV infections clear up on their own; it's the long-lasting ones, especially HPV 16 and 18, that can lead to abnormal cell changes and eventually cancer if undetected.[2] Current cervical cancer treatments focus on surgery, radiation, chemotherapy, targeted therapy, and immunotherapy, often combined based on cancer stage and type, with radiochemotherapy standard for advanced localized disease and chemo plus targeted drugs/immunotherapy for metastatic cases, plus clinical trials exploring new agents like sodomiden.[3] Nonetheless, current treatment methods still face challenges, including a high risk of recurrence, unintended damage to surrounding tissues, and the emergence of drug resistance.[4] Therefore, there is an urgent need to research better options like natural compounds, nanoparticles, and targeted immunotherapies, which aim for higher efficacy with fewer side effects to improve patient outcomes.

In recent years, the application of traditional Chinese medicine (TCM) in cervical cancer treatment has focused on its use as a complementary therapy to standard treatments. Research indicates that TCM helps to improve immune function, reduce the side effects of conventional treatments, and enhance patients' quality of life and survival rates.[5,6] Among these, phloroglucinol, a natural polyphenolic compound found in plants and marine brown algae, is being investigated in laboratory and preclinical studies for its potential anti-cancer effects, including its effects against cervical cancer cells.[7] The anti-cancer mechanism of phloroglucinol is multifaceted, primarily involving the induction of apoptosis and the inhibition of key cancer-related signaling pathways.[8,9] Bcl-2 protein is indeed the original, founding member of the Bcl-2 protein family, a critical anti-apoptotic protein that prevents programmed cell death (apoptosis) by regulating the mitochondria. Its discovery in lymphomas established the concept of defective apoptosis in cancer. It works by inhibiting pro-apoptotic members, preventing the release of cytochrome c, and thereby maintaining cell survival, playing a key role in development but also contributing to cancer when overexpressed.[10,11] Inhibiting anti-apoptotic members of the Bcl-2 family can reinstate normal apoptotic signaling, helping to counteract the resistance that cervical cancer cells often develop against conventional chemotherapy and radiotherapy.

Advancements in computational chemistry and bioinformatics are revolutionizing drug discovery, materials science, and personalized medicine by enabling faster and more accurate molecular modeling, virtual screening, genomic analysis, and the design of novel therapeutics. These fields allow the prediction of molecular properties, identification of disease markers, and optimization of drug formulations, thereby moving research from complex data to clinically relevant solutions.[12] The plant *Rhodomyrtus tomentosa* is widely utilized in traditional Vietnamese culture, where it is known as "sim". Roots and other parts are rich in

bioactive compounds, traditionally used across Asia to treat diarrhea, stomach issues, burns, inflammation, and even as a hemostatic agent. Scientific studies have explored its antioxidant, anti-inflammatory, and antibacterial properties, particularly highlighting compounds like rhodomyrtone for potential drug development.[13] A previous study on this species led to the isolation of several phloroglucinol derivatives with anti-cervical cancer activity against HeLa cell.[14] Despite these advances, the mechanisms of action of their bioactivity, particularly within apoptosis-regulatory pathways, remain underexplored. Therefore, an integrated computational approach was employed to assess both the interaction profiles and the mechanistic feasibility of the selected phloroglucinol derivatives. This study incorporated molecular docking, molecular dynamics simulations, MM/GBSA analyses, ADMET evaluation, and DFT-derived electronic parameters. Together, these results support the computational prioritization of candidates for further laboratory testing and structure-guided refinement in a cervical cancer–relevant context.

EXPERIMENTAL

Structural preparation of selected ligands

These selected phloroglucinol derivatives, including tomentodione S (CPD1), rhodomyrtosone I (CPD2), rhodomyrtone (CPD3), rhodomyrtosone B (CPD4), have molecular formulas of $C_{28}H_{30}O_6$, $C_{28}H_{30}O_6$, $C_{26}H_{34}O_6$, $C_{26}H_{34}O_6$, respectively, with molecular weights of 462.2042, 462.2042, 442.2355, 442.2355 Da. Belzutifan, possessing a molecular formula of $C_{17}H_{12}F_3NO_4S$ and a molecular weight of 383.0439 Da, was chosen as a reference compound (Fig. 1).
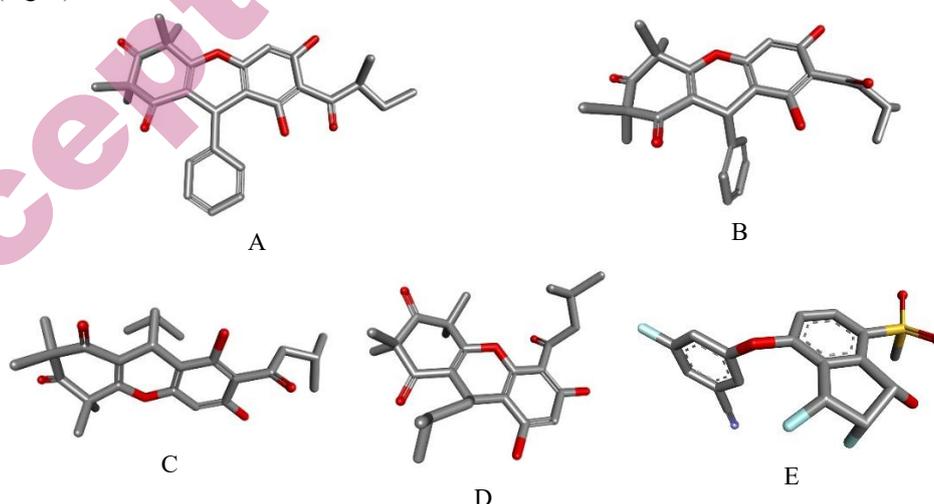

Fig. 1. Structure of the selected ligands. (A) CPD1, (B) CPD2, (C) CPD3, (D) CPD4, (E) Belzutifan.

Molecular docking study

Three-dimensional structures of the selected ligands were generated in BIOVIA Discovery Studio Visualizer and exported in PDB format. Before docking, polar hydrogens were incorporated, Gasteiger partial charges were assigned, and all rotatable bonds were left unconstrained to allow complete conformational freedom. The experimental structure of Bcl-2 (PDB ID: 6GL8) was obtained from the RCSB Protein Data Bank.[15] Docking calculations were carried out using AutoDock Tools,[16] employing a grid box with 60 points along each Cartesian axis and a grid spacing of 0.375 Å. The grid was positioned over the active site of the 6GL8 structure, centered at x = 9.866 Å, y = 0.590 Å, and z = 16.717 Å. Conformational exploration was conducted using the Lamarckian genetic algorithm, facilitating the identification of low-energy orientations and favorable interaction patterns. Ten independent GA–LS runs (ga_run = 10) were executed per ligand, with a population size of 150, a maximum of 2,500,000 energy evaluations, and 27,000 generations; Solis–Wets local search was enabled (300 iterations). Clustering of solutions used an RMS tolerance of 2.0 Å. AutoDock searches used stochastic initialization; the random seed handling followed the docking parameter files (seed = pid time). For each compound, the top-scoring pose was further inspected in Discovery Studio Client 2024 and compared to the docked configuration of Belzutifan on the same Bcl-2 template to evaluate correspondence in binding orientation and interaction characteristics.[17]

Molecular dynamics simulation

Molecular dynamics simulations were carried out on the top docking conformation of the ligand bound to the Bcl-2 protein (PDB ID: 6GL8) using GROMACS 2024.4 with the CHARMM36 force field applied under physiological conditions.[18] Before initiating the simulations, the protein structure was corrected in Swiss-PdbViewer, where missing atoms and unresolved residues were rebuilt to ensure structural completeness.[19] Ligand parameters compatible with the selected force field were produced via SwissParam.[20] The prepared complex was then positioned in a triclinic water box filled with SPC molecules, and the system's ionic strength was adjusted to 0.15 M NaCl to approximate physiological conditions. An initial energy minimization of 50,000 steps was performed to eliminate steric clashes and stabilize the system. Subsequent equilibration followed a two-stage routine: a 200 ps NVT phase to stabilize temperature, and a 200 ps NPT phase to equilibrate pressure, both maintained at 300 K and 1 bar. Temperature control was applied with the V-rescale thermostat ($\tau T = 0.1$ ps), using two coupling groups with reference temperatures of 300 K. Pressure coupling during NPT employed the Berendsen barostat (isotropic coupling; $\tau P = 2.0$ ps, reference pressure = 1.0 bar, compressibility = 4.5×10^{-5} bar^{-1}), while the production phase used the Parrinello–Rahman barostat (isotropic; $\tau P = 2.0$ ps, reference pressure = 1.0 bar, compressibility = 4.5×10^{-5} bar^{-1}). Production runs were executed as a single 100 ns simulation with a 2 fs time step; trajectory snapshots were recorded at 10 ns intervals for downstream analysis. Initial velocities were generated in the NVT stage from a Maxwell–Boltzmann distribution at 300 K with time-dependent seeding (gen_seed = −1). Electrostatics were treated with PME under the Verlet cutoff scheme (rlist = 1.2 nm; rcoulomb = 1.2 nm), and covalent bonds involving hydrogens were constrained with LINCS (h-bonds). Trajectory processing was performed using Grace to extract structural descriptors, root mean square deviation (RMSD), root mean square fluctuation (RMSF), radius of gyration (Rg), number of hydrogen bonds, and solvent-accessible surface area (SASA). Structural alignment in UCSF Chimera 1.13.3 was applied to compare representative conformations sampled along the trajectory and to assess overall complex stability. To investigate interaction durability, the ligand positions at the start (0 ns) and end (100 ns) of the simulation were superimposed within the binding pocket, allowing for the

assessment of the persistence of hydrogen bonding, hydrophobic contacts, and van der Waals interactions throughout the 100 ns simulation.[21]

Binding free energy calculation using MMGBSA

A binding free energy calculation for the CPD1–6GL8 and Belzutifan–6GL8 complexes was carried out using the gmx_MMPBSA protocol with the CHARMM36 force field.[22] The MMGBSA evaluation was performed as trajectory post-processing based on the same force-field description used in the molecular dynamics simulations, ensuring parameter consistency across the workflow. The electrostatic component of solvation was estimated through a generalized Born implicit-solvent model, while the nonpolar term was obtained from solvent-accessible surface area measurements. Energy decomposition was based on snapshots extracted from the molecular dynamics trajectories between 20 and 100 ns, resulting in an 80-ns analysis interval. A total of 125 frames, selected at uniform 80 ps intervals, were used to ensure representative sampling of complex behavior. This ensemble-averaged approach enabled a direct comparison of the binding energetics of the two ligands, providing insight into differences in affinity and the dynamic stability of each complex over the examined simulation.

ADMET prediction

Evaluation of absorption, distribution, metabolism, excretion, and toxicity (ADMET) parameters represents a core element of preclinical screening, as it facilitates early identification of pharmacokinetic constraints and potential safety liabilities. Such an appraisal can mitigate attrition during advanced development stages and enhance the prioritization of candidates exhibiting more favorable therapeutic promise. In this study, the pkCSM framework was applied to estimate the ADMET profiles of CPD1 and Belzutifan computationally. The pkCSM approach derives predictions from graph-based molecular signatures, thereby enabling a systematic assessment of key biopharmaceutical and toxicological properties of the investigated compounds.[23]

Quantum DFT analysis

Structural minimization of CPD1 and belzutifan was conducted using the ORCA quantum chemistry suite (v6.1.0). Initial geometries were prepared using Avogadro, while molecular orbital visualisation and related electronic analyses were completed with IboView (v20211019).[24–26] Density functional theory computations employed the B3LYP exchange–correlation functional together with the 6-31G(d,p) basis set to yield internally consistent electronic wavefunctions. Based on the converged, fully optimised geometries, quantum-chemical descriptors were derived, comprising the highest occupied molecular orbital (HOMO) and lowest unoccupied molecular orbital (LUMO) energies, the HOMO–LUMO separation (ΔE), chemical potential (μ), electronegativity (χ), global hardness (η), softness (σ), and electrophilicity index (ω). Interpretation of these quantities followed the Koopmans' theorem approximation to characterise electronic structure and to support inference regarding the intrinsic reactivity of the studied molecules.[27,28]

RESULTS AND DISCUSSION

Molecular docking analysis

Molecular docking constitutes a computational strategy for modelling the association between a low-molecular-weight ligand and a macromolecular target, such as a protein, to estimate the preferred binding orientation and the corresponding interaction strength. This approach supports a mechanistic

interpretation of molecular recognition and is widely applied in structure-based drug discovery to relate binding propensity to biological response. Docking protocols typically integrate conformational and positional sampling algorithms to explore candidate binding modes, followed by scoring functions that approximate the energetic favorability of each configuration. The highest-ranked solutions represent putative stable complexes with comparatively low estimated free energy and enhanced structural complementarity.[29] Before docking the selected ligands into the Bcl-2 structure (PDB ID: 6GL8), the reliability of the docking workflow was examined through a re-docking exercise using the ligand co-resolved in the crystallographic complex (Fig. 2). The optimal re-docked pose reproduced the experimentally reported binding orientation within the predefined binding region with an RMSD of 0.7540 Å, indicating that the grid definition and search settings were appropriate for describing the 6GL8 pocket. In standard docking practice, successful recovery of the co-crystallized pose with a root-mean-square deviation (RMSD) below 2 Å is generally interpreted as evidence of acceptable protocol performance and pose predictability.[30] Following this validation step, all ligand poses were scored and ranked according to predicted binding energy, where more negative values reflect a stronger estimated binding preference.

Fig. 2. The superimposition of the docked and native ligands within 6GL8 protein for validation of the molecular docking protocol (yellow = native, violet = docked).

As reported in Table 1, docking scores and residue-level contacts were examined for four candidate ligands (CPD1–CPD4) within a pocket repeatedly defined by Phe104, Tyr108, Asp111, Phe112, Gln118, Leu137, Ala149, and Phe153. Belzutifan was included as the reference compound under the same scoring scheme. Across the evaluated complexes, the contact pattern indicated an aromatic–aliphatic cavity dominated by Phe/Tyr side chains, complemented by polar residues (Asp111, Gln118, and Glu136) that may contribute to directional stabilization through hydrogen bonding. Predicted binding energies ranged from -37.36 to -25.73 kJ/mol, supporting a clear affinity ranking of CPD1 > CPD2 >

CPD3 > CPD4 > Belzutifan. The interaction inventory comprised hydrogen bonding, van der Waals contacts, and hydrophobic interactions, as annotated for each ligand–target complex. Collectively, these non-covalent forces are expected to promote complex integrity through (i) directional hydrogen-bond constraints that stabilize specific geometries via alignment with electronegative centers, (ii) hydrophobic clustering that limits solvent accessibility and favors compact packing within the binding cavity, and (iii) short-range van der Waals complementarity that contributes incremental stabilization while fine-tuning association energetics and kinetic persistence.[31,32]
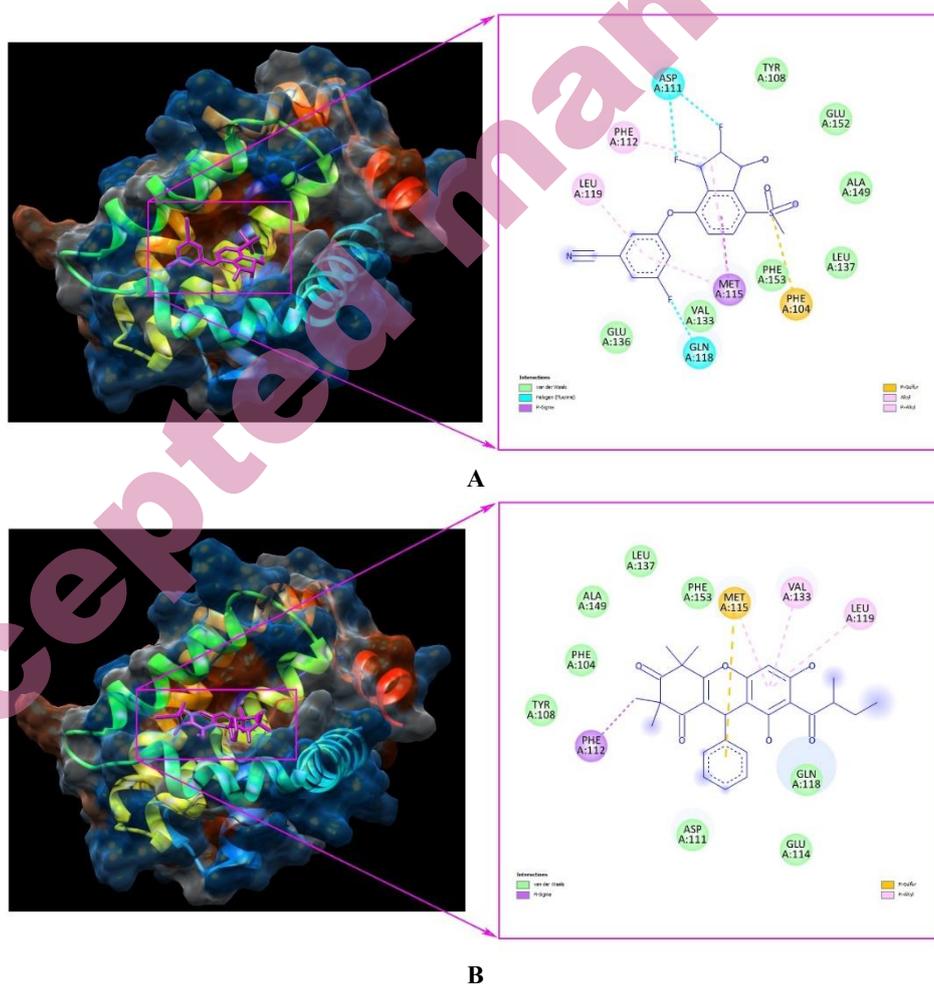

A

B

Fig. 3. Molecular docking model and 2D interaction diagram of CPD1 (A) and Belzutifan (B) with 6GL8 protein.

CPD1 produced the most favorable docking energy (-37.36 kJ/mol) and engaged the complete canonical residue set (Phe104, Tyr108, Asp111, Phe112, Gln118, Leu137, Ala149, Phe153). No hydrogen bond was annotated; instead, stabilization was characterized by extensive van der Waals complementarity (Phe104, Tyr108, Asp111, Glu114, Gln118, Leu137, Ala149, Phe153) together with hydrophobic contacts involving Phe112, Met115, Leu119, and Val133, consistent with tight packing inside the pocket (Fig. 3A).

CPD2 displayed the second-highest affinity (-33.14 kJ/mol) while retaining most core contacts (Phe104, Tyr108, Asp111, Phe112, Gln118, Leu137, Ala149). A hydrogen bond to Glu136 was recorded, accompanied by van der Waals interactions with Phe104, Tyr108, Glu114, Gln118, Leu137, and Ala149 and additional hydrophobic contributions from Asp111, Phe112, Met115, Leu119, and Val133. The absence of Phe153 among the listed active-site contacts suggests a slightly reduced engagement of the distal aromatic boundary relative to CPD1.

CPD3 yielded an intermediate docking score (-32.38 kJ/mol) and contacted Phe104, Phe112, Gln118, Leu137, Ala149, and Phe153. Two hydrogen bonds were assigned (Gln118 and Glu136), and the van der Waals network extended toward Leu119, Arg129, and Thr132 in addition to Phe104, Phe112, Ala149, and Phe153, indicating a pose with measurable polar anchoring yet a shifted contact distribution. Hydrophobic interactions were primarily associated with Met115, Val133, and Leu137.

TABLE I. The interactions between the docked ligands and the protein 6GL8.

Docked ligands	Binding energy (kJ/mol)	Hydrogen bond interaction	Van der Waals interaction	Hydrophobic interaction
CPD1	-37.36	-	Phe104, Tyr108, Asp111, Glu114, Gln118, Leu137, Ala149, Phe153	Phe112, Met115, Leu119, Val133
CPD2	-33.14	Glu136	Phe104, Tyr108, Glu114, Gln118, Leu137, Ala149	Asp111, Phe112, Met115, Leu119, Val133
CPD3	-32.38	Gln118, Glu136	Phe104, Phe112, Leu119, Arg129, Thr132, Ala149, Phe153	Met115, Val133, Leu137
CPD4	-30.42	-	Phe104, Tyr108, Asp111, Gln118, Leu119, Val133, Leu137, Glu152, Val156	Phe112, Met115, Ala149, Phe153
Belzutifan	-25.73	-	Tyr108, Val133, Glu136, Leu137, Ala149, Glu152, Phe153	Phe104, Asp111, Phe112, Met115, Gln118, Leu119

CPD4 exhibited a lower predicted affinity (-30.42 kJ/mol) despite preservation of the canonical active-site residues (Phe104, Tyr108, Asp111, Phe112, Gln118, Leu137, Ala149, Phe153). No hydrogen bond was annotated.

Van der Waals contacts included the core residues and additional interactions with Leu119, Val133, Glu152, and Val156. At the same time, hydrophobic contributions involved Phe112, Met115, Ala149, and Phe153, suggesting that nonpolar and dispersive terms dominated binding stabilization without explicit polar locking.

Belzutifan showed the weakest docking energy (-25.73 kJ/mol) while maintaining contact with the conserved pocket residues (Phe104, Tyr108, Asp111, Phe112, Gln118, Leu137, Ala149, Phe153). The interaction map lacked hydrogen bonding and was defined by van der Waals contacts (Tyr108, Val133, Glu136, Leu137, Ala149, Glu152, Phe153) plus hydrophobic interactions (Phe104, Asp111, Phe112, Met115, Gln118, Leu119) (Fig. 3B).

Overall, CPD1 emerged as the highest-priority ligand in the docking series, exhibiting the most favorable binding energy (-37.36 kJ/mol) and extensive engagement of the conserved binding pocket (Phe104, Tyr108, Asp111, Phe112, Gln118, Leu137, Ala149, and Phe153). The predicted pose was stabilized predominantly by dense van der Waals complementarity with the core residues and additional hydrophobic packing involving Phe112, Met115, Leu119, and Val133, indicating tight accommodation within the aromatic–aliphatic cavity. On this basis, CPD1 was selected as the highest-priority candidate for subsequent molecular dynamics simulations to evaluate the time-dependent persistence of its pose and the stability of its principal contact network under protein flexibility and solvent effects.

Molecular dynamics simulation

Drug-likeness screening, molecular docking, and molecular dynamics simulations form a complementary in silico pipeline for structure-based drug discovery. Drug-like filters narrow chemical space, docking rapidly proposes and ranks binding poses, and molecular dynamics provides time-resolved trajectories that capture conformational fluctuations and intermolecular interactions by integrating classical equations of motion on a potential-energy surface. In this context, molecular dynamics extends docking by testing pose stability in a dynamic, solvated environment, evaluating persistence of key contact and hydrogen-bond networks, and supporting more reliable energetic characterization for hit validation and lead optimization.[33] Therefore, the evaluation systematically investigated RMSD, RMSF, Rg, Hbonds, and SASA metrics to determine the stability, flexibility, and solvent exposure of the CPD1-6GL8 and Belzutifan-6GL8 complexes throughout the simulation. Because one 100 ns production trajectory was analyzed for each complex, these MD metrics should be interpreted as qualitative descriptors of trajectory behavior rather than statistically averaged results from replicate simulations. Consequently, the total energy and potential energy values for the CPD1-6GL8 complex were found to be -227,913 kJ/mol and -282,916 kJ/mol, respectively. For the Belzutifan-6GL8 complex, the total energy

and potential energy values were measured at -227,574 kJ/mol and -282,502 kJ/mol, respectively. The simulation system maintained equilibrium at a temperature of 300 K.

The RMSD describes the extent of structural displacement relative to a reference after optimal superposition and is routinely used to monitor equilibration and global stability during molecular dynamics simulations.[34] In the present trajectories, both complexes exhibited an early accommodation phase followed by confinement within a narrow RMSD band, without sustained divergence across the 0–100 ns interval. The CPD1–6GL8 profile fluctuated predominantly around the 0.18–0.24 nm region, with intermittent excursions approaching 0.25 nm, whereas the Belzutifan–6GL8 profile occupied a similar interval but displayed more frequent high-RMSD episodes (reaching 0.25–0.26 nm), particularly in the late-stage segment (Fig. 4A). The close overlap of both traces and the absence of progressive drift support preservation of the overall protein conformation under both ligand-bound conditions. To quantify late-stage equilibration, plateau RMSD values were defined as the time-averaged RMSD over the final 30 ns of the trajectories (70–100 ns). The plateau RMSD was 0.204 ± 0.014 nm for CPD1–6GL8 and 0.217 ± 0.013 nm for Belzutifan–6GL8, where the standard deviation reflects fluctuations within this plateau window of a single trajectory.

The RMSF quantifies residue-level mobility around the time-averaged position, thereby identifying locally flexible segments and relatively rigid cores. Within the Gly7–Gly203 interval, the RMSF profiles of both the CPD1–6GL8 and Belzutifan–6GL8 complexes are low in amplitude and nearly superimposable, indicating a structurally stable N-terminal region beyond the highly mobile initial residues. After the sharp fluctuation at the beginning of the sequence, RMSF values rapidly decrease and remain consistently low throughout this interval, generally around 0.04–0.06 nm, and rarely exceed 0.07–0.08 nm (Fig. 4B). No pronounced flexibility peaks or ligand-dependent deviations are observed in this region, suggesting that ligand binding has minimal impact on local dynamics within Gly7–Gly203, which behaves as a relatively rigid structural core in both simulations.

Rg reflects the mass-weighted spatial distribution of atoms around the center of mass and serves as a measure of global compactness. Both systems demonstrated an early relaxation from the 1.46 nm region toward 1.44 nm, followed by sustained oscillations within a constrained interval. The CPD1–6GL8 trajectory remained approximately within 1.42–1.46 nm, while Belzutifan–6GL8 generally occupied 1.42–1.47 nm and included a rare transient expansion close to 1.48 nm (Fig. 4C). A mild upward shift for Belzutifan–6GL8 during 70–95 ns was evident relative to CPD1–6GL8, consistent with slightly reduced compactness in the reference-bound state during that period.

Intermolecular hydrogen bonds provide directional constraints that can enhance binding specificity and contribute to dynamic stability, although hydrophobic and dispersive interactions frequently supply substantial stabilization in ligand–protein complexes.[35] The CPD1–6GL8 complex exhibited hydrogen-bond counts spanning 0–3, with the trajectory most commonly occupying 0–2 bonds and a short-lived event reaching three near the early-mid portion of the simulation (Fig. 4D). Belzutifan–6GL8 fluctuated mainly between 0 and 2 hydrogen bonds, with extended intervals dominated by a single bond and intermittent two-bond events. The comparative pattern indicates that CPD1 maintained a slightly broader polar-contact repertoire, while a more consistently sparse hydrogen-bond regime characterized Belzutifan.

The SASA reports the degree of solvent exposure and can reflect changes in global packing and surface rearrangements during molecular dynamics. Both systems displayed bounded SASA fluctuations across the entire trajectory (80–92 nm²), without a monotonic drift suggestive of unfolding (Fig. 4E). A modest separation emerged after 70 ns, where CPD1–6GL8 tended toward higher SASA values and larger excursions, while Belzutifan–6GL8 showed a comparatively lower envelope over the same interval, indicating subtle differences in solvent exposure despite broadly stable global architecture.

Collectively, RMSD and Rg traces support sustained structural integrity for both ligand-bound states across 100 ns, with CPD1–6GL8 exhibiting slightly tighter late-stage confinement in global measures and a marginally richer hydrogen-bonding pattern. The RMSF distribution indicates that ligand-dependent effects were localized rather than systemic, consistent with stable binding accompanied by limited loop reorganization. When considered alongside the stronger docking score previously obtained for CPD1, the MD readouts provide convergent support for prioritization of CPD1 as the more favorable 6GL8 binder under the simulated conditions.

Free binding energy (MMGBSA) analysis

MMGBSA (Molecular Mechanics/Generalized Born Surface Area) is a commonly applied approach in computational biochemistry and drug design for approximating the binding free energy of a ligand–macromolecule complex. The method integrates molecular mechanics energy terms with an implicit-solvent treatment, where the Generalized Born model represents electrostatic solvation and a solvent-accessible surface area term accounts for nonpolar contributions. By post-processing molecular dynamics trajectories rather than relying on fully explicit solvent-free energy protocols, MMGBSA provides a comparatively efficient route to ranking binding affinities while retaining physically interpretable energy components.
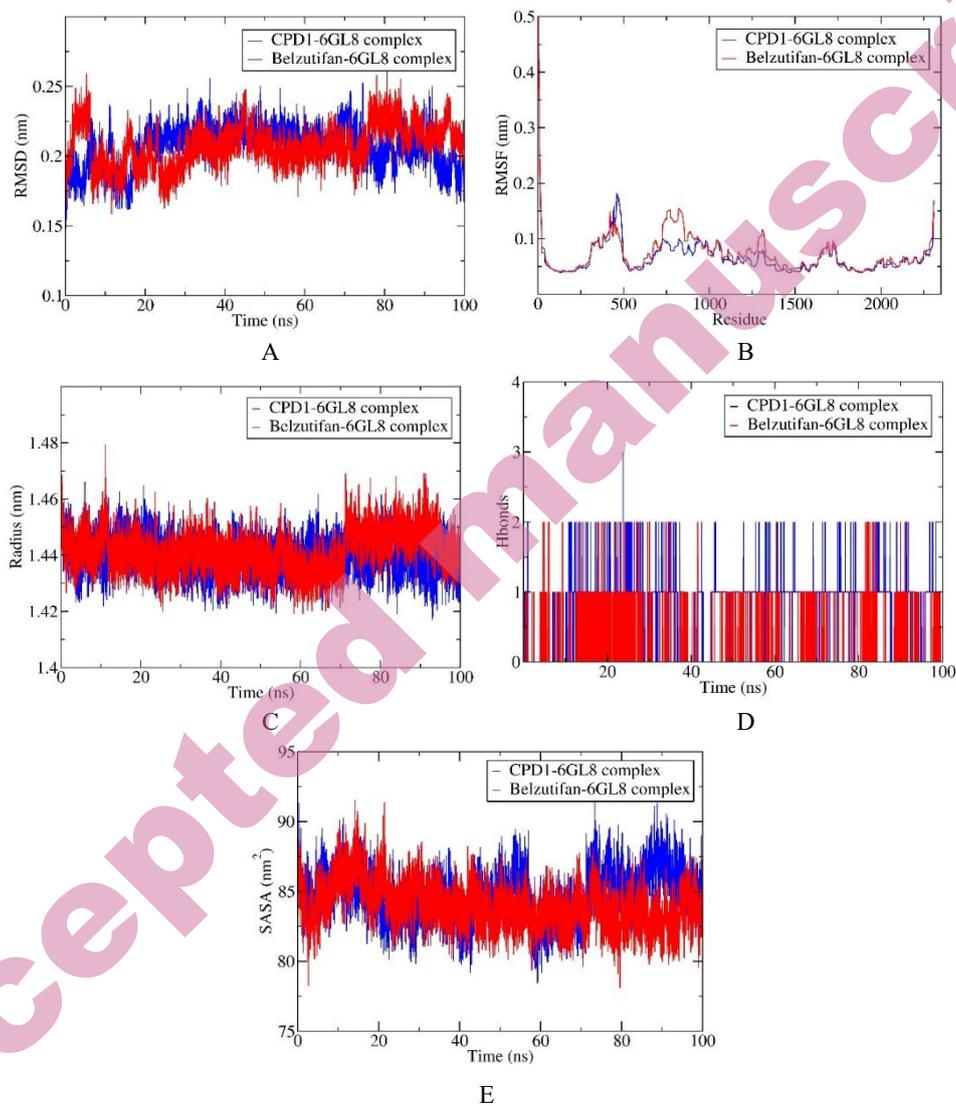
Fig. 4. Results of MD simulation for the bindings of CPD1 (blue) and Belzutifan (red) with 6GL8 protein. (A) RMSD, (B) RMSF, (C) Rg, (D) Hbonds, and (E) SASA.

TABLE II. Free energy of binding obtained using MMGBSA calculations.

Energy component	Average (kJ/mol)		Standard Deviation	
	CPD1-6GL8	Belzutifan-6GL8	CPD1-6GL8	Belzutifan-6GL8
ΔVDWAΔALS	-156.57	-131.46	14.85	16.44
ΔEEL	-101.92	-52.01	39.83	35.77
ΔEGB	141.88	138.91	28.53	35.10
ΔESURF	-22.13	-19.16	1.84	2.30
ΔGGAS	-258.49	-183.47	38.79	41.59
ΔGSOLV	119.75	119.75	27.91	34.18
ΔTOTAL	-138.78	-63.72	15.40	14.31

Binding free energies for the CPD1–6GL8 and Belzutifan–6GL8 complexes were assessed using the MM/GBSA approach. In this analysis, the reported binding term represents an enthalpy-dominated estimate because configurational entropy was not included; nevertheless, such treatment remains appropriate for comparative ranking between closely related protein–ligand systems. The mean values and corresponding standard deviations describe the interplay between gas-phase stabilization, arising from van der Waals and electrostatic interactions, and the opposing (or compensating) influence of solvation, captured by polar and nonpolar solvent contributions, thereby enabling mechanistic interpretation through energy-component decomposition. Both systems display a favorable association, as indicated by negative total binding energies. Configurational entropy ($-T\Delta S$) was intentionally not included in the present MMGBSA post-processing; therefore, the reported ΔTOTAL values should be interpreted as enthalpy-dominated (ΔH-like) estimates rather than full binding free energies (ΔG). As detailed in Table 2, CPD1–6GL8 shows a markedly more favorable mean ΔTOTAL of -138.78 ± 15.4 kJ/mol relative to Belzutifan–6GL8 (-63.72 ± 14.31 kJ/mol), corresponding to an advantage of 75.06 kJ/mol for CPD1. This separation is primarily attributed to stronger gas-phase interactions for CPD1, with ΔGGAS reaching -258.49 ± 38.79 kJ/mol, compared with -183.47 ± 41.59 kJ/mol for Belzutifan. Within the gas-phase term, electrostatics contribute substantially to the difference: ΔEEL is more stabilizing for CPD1 (-101.92 ± 39.83 kJ/mol) than for Belzutifan (-52.01 ± 35.77 kJ/mol). Van der Waals interactions remain favorable for both ligands and further support CPD1 binding (ΔVDWAΔALS = -156.57 ± 14.85 kJ/mol versus -131.46 ± 16.44 kJ/mol). In contrast, the overall solvation contribution is identical in mean magnitude for both complexes (ΔGSOLV = 119.75 ± 27.91 kJ/mol for CPD1 and 119.75 ± 34.18 kJ/mol for Belzutifan). This equality reflects rounding at the reported precision, because ΔGSOLV is obtained as ΔEGB + ΔESURF and the component means differ slightly between systems but yield the same rounded sum. Consistently, the polar solvation term is comparable (ΔEGB = 141.88 ± 28.53 kJ/mol for CPD1; 138.91 ± 35.10 kJ/mol for Belzutifan), whereas the nonpolar component is slightly more favorable for CPD1

(ΔESURF = -22.13 $\pm$ 1.84 kJ/mol) than for Belzutifan (-19.16 $\pm$ 2.3 kJ/mol). Variability in the total binding estimate remains similar between systems, with standard deviations of 15.40 and 14.31 kJ/mol for CPD1 and Belzutifan, respectively, indicating a consistent energetic preference for CPD1, primarily driven by stronger gas-phase stabilization, particularly electrostatic complementarity.

ADMET prediction analysis

In silico ADMET profiling was conducted to characterize the predicted pharmacokinetic behavior and safety-relevant alerts of CPD1 in comparison with the reference compound Belzutifan, with descriptors organized into absorption, distribution, metabolism, excretion, and toxicity domains. This side-by-side evaluation provides an integrated basis for identifying potential liabilities and prioritizing candidates within an in silico modeling framework focused on selected phloroglucinol derivatives from *Rhodomyrtus tomentosa* and their prospective utility against cervical cancer.[36] The predicted ADMET parameters for CPD1 and Belzutifan are summarized in Table 3.

Regarding absorption, both molecules exhibit closely matched predicted aqueous solubility, with water solubility values of -4.749 log mol/L for CPD1 and -4.733 log mol/L for Belzutifan, indicating comparably limited dissolution under the applied model. Membrane permeability, however, differentiates the profiles: Belzutifan presents higher Caco-2 permeability (1.282 log Papp in 10^{-6} cm/s) than CPD1 (1.109), whereas CPD1 shows stronger predicted human intestinal absorption (98.254%) relative to Belzutifan (92.996%). Skin permeability estimates remain similar, with log Kp values of -2.736 for CPD1 and -2.784 for Belzutifan. Transporter-related annotations further distinguish the compounds, as CPD1 is predicted to be a P-glycoprotein substrate, whereas Belzutifan is not. Both compounds are flagged as P-glycoprotein I inhibitors; however, only CPD1 is expected to inhibit P-glycoprotein II.

Distribution descriptors indicate divergent systemic disposition tendencies. A lower predicted steady-state volume of distribution is observed for CPD1 (VDss = -0.152 log L/kg) compared with Belzutifan (0.684 log L/kg), consistent with a more constrained distributional extent for CPD1 within this output. The predicted unbound fraction in human plasma is higher for CPD1 (Fu = 0.035) than for Belzutifan (0.014), suggesting greater free-drug availability for CPD1 according to the model. Central exposure indices also differ: BBB permeability is positive for CPD1 (log BB = 0.192) but strongly negative for Belzutifan (-1.105), and CNS permeability follows the same directionality, with CPD1 showing less negative log PS (-2.605) than Belzutifan (-3.167), indicating comparatively higher predicted central penetration for CPD1. Because BBB penetration is not a therapeutic requirement for cervical cancer, the positive BBB permeability prediction for

CPD1 is discussed primarily as a distribution/safety consideration rather than a clinical advantage.

TABLE III. Predicted ADMET properties of CPD1 and Belzutifan.

ADMET properties	Unit	CPD1	Belzutifan
Water Solubility	(Log mol/L)	-4.749	-4.733
Caco2 permeability	(Log Papp in 10-6 cm/s)	1.109	1.282
Intestinal absorption (Human)	(% Absorbed)	98.254	92.996
Skin permeability	(Log Kp)	-2.736	-2.784
P-glycoprotein substrate	Yes/No	Yes	No
P-glycoprotein I inhibitor	Yes/No	Yes	Yes
P-glycoprotein II inhibitor	Yes/No	Yes	No
VDss	(Log L/kg)	-0.152	0.684
Fraction unbound (human)	(Fu)	0.035	0.014
BBB permeability	(Log BB)	0.192	-1.105
CNS permeability	(Log PS)	-2.605	-3.167
CYP2D6 substrate	Yes/No	No	No
CYP3A4 substrate	Yes/No	Yes	Yes
CYP1A2 inhibitor	Yes/No	No	Yes
CYP2C19 inhibitor	Yes/No	Yes	Yes
CYP2C9 inhibitor	Yes/No	Yes	Yes
CYP2D6 inhibitor	Yes/No	No	No
CYP3A4 inhibitor	Yes/No	No	No
Total clearance	(Log ml/min/kg)	0.212	0.291
Renal OCT2 substrate	Yes/No	No	No
AMES toxicity	Yes/No	No	No
Max. tolerated dose (human)	(Log mg/kg/day)	-0.049	0.291
hERG I inhibitor	Yes/No	No	No
hERG II inhibitor	Yes/No	Yes	No
Oral rat acute toxicity (LD50)	(mol/kg)	2.543	2.775
Oral rat chronic toxicity (LOAEL)	(Log mg/kg_bw/day)	1.618	0.892
Hepatotoxicity	Yes/No	No	Yes
Skin sensation	Yes/No	No	No
Tetrahymena pyriformis toxicity	(Log ug/L)	0.292	0.419
Minnow toxicity	(Log mM)	-0.89	1.344

Metabolism-related predictions highlight shared and distinct CYP interaction patterns. Neither compound is categorized as a CYP2D6 substrate, while both are predicted CYP3A4 substrates. Inhibitory flags overlap for CYP2C19 and CYP2C9, which are positive for both CPD1 and Belzutifan. A key divergence is seen for CYP1A2 inhibition, which is negative for CPD1 but positive for Belzutifan. No inhibition is predicted for CYP2D6 or CYP3A4 in either compound under the same settings.

Excretion estimates indicate a modestly higher predicted total clearance for Belzutifan (0.291 log ml/min/kg) compared to CPD1 (0.212 log ml/min/kg). Renal

OCT2 substrate status is negative for both ligands, indicating no OCT2-associated renal transport designation in the present output.

Toxicity endpoints reveal both shared reassurance signals and notable compound-specific alerts. AMES toxicity and hERG I inhibition are negative for both CPD1 and Belzutifan. In contrast, hERG II inhibition is predicted for CPD1 but not for Belzutifan, indicating a differential cardiac liability flag in this dataset. The predicted hERG II inhibition flag for CPD1 is an in silico alert (pkCSM-based) and should not be interpreted as confirmed cardiotoxicity; experimental electrophysiology assays would be required to validate this risk. Hepatotoxicity is expected to be negative for CPD1 and positive for Belzutifan, representing a prominent separation in safety-relevant alerts. Quantitative indices further differentiate tolerability and toxicity: the maximum tolerated dose (human) is -0.049 log mg/kg/day for CPD1 and 0.291 for Belzutifan; oral rat acute toxicity (LD50) is 2.543 mol/kg for CPD1 and 2.775 mol/kg for Belzutifan; oral rat chronic toxicity (LOAEL) is higher for CPD1 (1.618 log mg/kg_bw/day) than for Belzutifan (0.892). Skin sensitization is negative for both. Ecotoxicity-associated descriptors indicate higher predicted *Tetrahymena pyriformis* toxicity for Belzutifan (0.419 log μg/L) than CPD1 (0.292), while minnow toxicity differs markedly, with CPD1 at -0.89 log mM and Belzutifan at 1.344 log mM.

Overall, the ADMET output indicates broadly similar solubility and dermal permeability for CPD1 and Belzutifan, while suggesting higher intestinal absorption for CPD1, despite its lower Caco-2 permeability. Distributional behavior differs substantially, with CPD1 exhibiting lower VDss yet higher predicted unbound fraction and less restricted BBB/CNS permeability compared with Belzutifan. Metabolic interaction potential overlaps through CYP3A4 substrate status and CYP2C19/CYP2C9 inhibition, whereas a CYP1A2 inhibition flag is restricted to Belzutifan. Safety-related predictions indicate an absence of hepatotoxicity for CPD1, alongside a hepatotoxicity alert for Belzutifan. A hERG II inhibition flag emerges for CPD1, but not for Belzutifan. These distinctions provide a mechanistic basis for prioritization and risk awareness in subsequent computational and experimental validation of phloroglucinol-derived candidates targeting cervical cancer–relevant pathways.

Quantum chemistry computation using the DFT method

Density Functional Theory is indeed crucial for natural compounds and drug design, as it helps predict molecular structures, properties, binding affinities to targets, reaction pathways, and simulate interactions. This speeds up the discovery of new medicines from nature by understanding how molecules work and fit together, optimizing lead compounds, and reducing experimental costs.[37] DFT calculations were thus performed, following the classical modeling workflow, to characterize the electronic structure and infer reactivity-associated features of CPD1 relative to the reference compound, Belzutifan. The computed set included

EHOMO (eV), ELUMO (eV), ΔE (eV), μ (eV), χ (eV), η (eV), σ (eV-1), and ω (eV), collectively describing frontier-orbital energetics, resistance to charge redistribution, and electrophilic behavior. Within this context, EHOMO (eV) (highest occupied molecular orbitals) relates to electron-donating propensity, whereas ELUMO (eV) (lowest unoccupied molecular orbitals) reflects electron-accepting capacity; the ΔE (eV) (energy gap) between these orbitals serves as an indicator of electronic stability versus chemical responsiveness.[38]

TABLE IV. DFT calculations for CPD1 and Belzutifan.

Molecule	EHOMO (eV)	ELUMO (eV)	ΔE (eV)	μ (eV)	χ (eV)	η (eV)	σ (eV-1)	ω (eV)
CPD1	-7.7313	-4.7815	2.9498	-6.2564	6.2564	1.4749	0.6780	13.2696
Belzutifan	-9.9400	1.3289	11.2689	-4.3056	4.3056	5.6345	0.1775	1.6450

EHOMO (eV): highest occupied molecular orbitals; ELUMO (eV): lowest unoccupied molecular orbitals; ΔE (eV): energy gap; μ (eV): chemical potential; χ (eV): electronegativity; η (eV): hardness; σ (eV-1): softness; ω (eV): electrophilicity index.
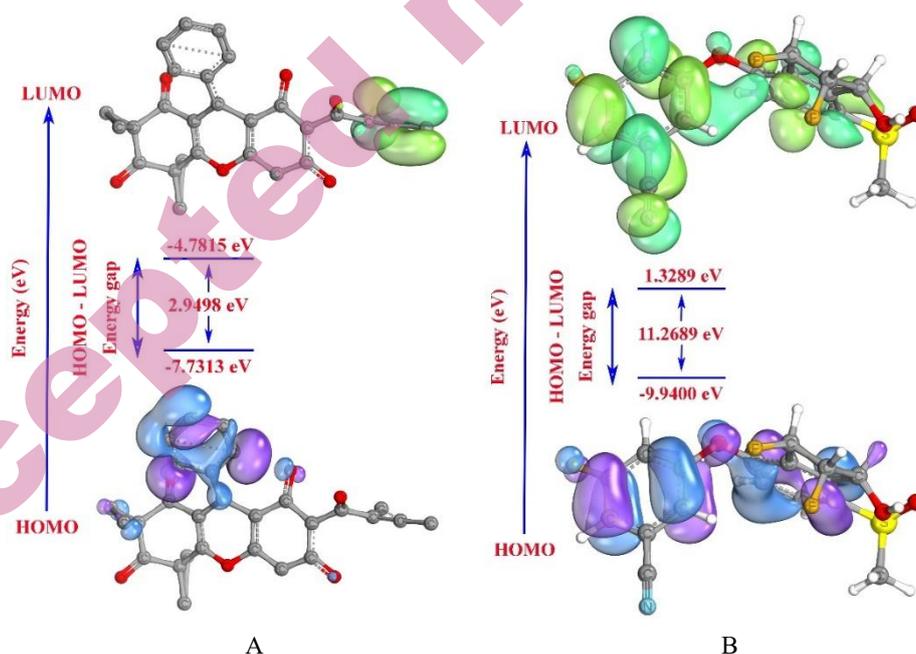

Fig. 5. HOMO and LUMO surface diagrams of CPD1 (A) and Belzutifan (B).

For CPD1, EHOMO (eV) is -7.7313, higher than the value obtained for Belzutifan (-9.9400), supporting a comparatively greater tendency toward electron donation under the applied computational conditions (Table 4). A pronounced divergence is observed for ELUMO (eV), where CPD1 retains a negative value (-4.7815) while Belzutifan exhibits a positive ELUMO (eV) of 1.3289, consistent

with a substantially lower-lying acceptor orbital for CPD1. In accordance with these frontier-orbital positions, CPD1 presents a markedly smaller ΔE (eV) of 2.9498 relative to Belzutifan (11.2689). This pattern aligns with enhanced electronic polarizability and higher potential chemical responsiveness for CPD1, whereas the wider gap in Belzutifan is consistent with greater stabilization of frontier orbitals. Global descriptors further reinforce these differences. Electronegativity χ (eV) is higher for CPD1 (6.2564) than for Belzutifan (4.3056), accompanied by a more negative chemical potential μ (eV) for CPD1 (-6.2564) compared with Belzutifan (-4.3056), reflecting the expected inverse correspondence between μ (eV) and χ (eV) within this descriptor set. Hardness η (eV) is substantially lower for CPD1 (1.4749) than for Belzutifan (5.6345). The reciprocal softness σ (eV-1) is consequently higher for CPD1 (0.6780) than for Belzutifan (0.1775), indicating reduced resistance to electron-density deformation for CPD1 (Fig. 5). Finally, the electrophilicity index ω (eV) is markedly elevated for CPD1 (13.2696) relative to Belzutifan (1.6450), indicating a stronger electrophilic character for CPD1 in the present DFT dataset.

Frontier-orbital and global reactivity indices primarily reflect intrinsic electronic responsiveness and should not be interpreted as stand-alone predictors of anticancer activity. Here, the smaller ΔE and higher ω of CPD1 are viewed as facilitating polarization and charge redistribution upon complexation, which aligns with the more favorable gas-phase contribution, especially ΔEEL, observed in the MM/GBSA decomposition. This electronic context complements the docking/MD observation that CPD1 is stabilized largely by dispersive and hydrophobic packing within the 6GL8 cavity, while experimental validation remains necessary to link electronic descriptors to biological response. A formal correlation analysis between DFT descriptors and binding energies was not performed in the present dataset; accordingly, any linkage between electronic indices and binding behavior is discussed as a qualitative rationale rather than a demonstrated relationship.

CONCLUSION

This work integrated molecular docking, molecular dynamics, MMGBSA, ADMET prediction, and DFT descriptors to evaluate phloroglucinol derivatives from *R. tomentosa* against the 6GL8 target in a cervical cancer–relevant context. CPD1 consistently ranked highest, showing the best docking score (-37.36 kJ/mol) versus Belzutifan (-25.73 kJ/mol) with extensive engagement of the conserved pocket, and stable MD behavior over 100 ns. MMGBSA supported stronger binding for CPD1 (ΔTOTAL = -138.78 ± 15.4 kJ/mol) than Belzutifan (-63.72 ± 14.31 kJ/mol), driven by more favorable gas-phase interactions (ΔGGAS = -258.49 ± 38.79 vs -183.47 ± 41.59 kJ/mol) while ΔGSOLV remained equal (119.75 kJ/mol). ADMET outputs indicated similar solubility but higher intestinal absorption for CPD1, alongside distinct safety/transport alerts (hepatotoxicity

negative yet hERG II positive for CPD1; hepatotoxicity positive yet hERG II negative for Belzutifan). DFT further characterized CPD1 by a smaller ΔE (2.9498 vs 11.2689 eV) and higher ω (13.2696 vs 1.6450 eV), supporting greater electrophilic character, which is interpreted as an electronic-property context for binding energetics rather than a direct surrogate for biological potency, and is presented as supportive electronic context in the absence of correlation analysis.

Despite the utility of computational screening for triaging candidates, experimental confirmation remains essential to establish the translational robustness of findings. A further limitation of this study is that Belzutifan, although used here as a reference compound under the same computational protocol, is not a canonical Bcl-2 inhibitor. Therefore, comparisons against Belzutifan should be interpreted cautiously and not as equivalent to benchmarking against a target-validated Bcl-2 inhibitor. No in vitro or in vivo validation is available within the present dataset, limiting inference beyond the predicted binding and property space. Future work should prioritize biochemical target-engagement assays, cell-based efficacy testing in cervical cancer models, and safety-oriented profiling that addresses electrophysiology-relevant endpoints, hepatic liability, and absorption, distribution, metabolism, and excretion (ADME) behavior. Additional limitations include the absence of an explicit entropic term in MMGBSA and the lack of dedicated evaluation of off-target or unintended covalent mechanisms. If subsequent experimental studies corroborate potency and an acceptable safety margin, progression toward more advanced preclinical characterization would be justified, with the current computational results providing a mechanistic foundation to guide rational follow-up and lead optimization.

И З В О Д

IN SILICO МОДЕЛОВАЊЕ ОДАБРАНИХ ФЛОРОГЛУЦИНОЛСКИХ ДЕРИВАТА ИЗ RHODOMYRTUS TOMENTOSA: МЕХАНИСТИЧКИ УВИД У ЊИХОВ ПОТЕНЦИЈАЛ ПРОТИВ КАРЦИНОМА ГРЛИЋА МАТЕРИЦЕ

HUNG DUC NGUYEN

Thai Nguyen University of Education, 24000 Thai Nguyen, VietNam.

Карцином грлића материце остаје један од водећих узрока оболевања и смртности на глобалном нивоу, а примарни покретач је перзистентна инфекција високо-ризичним типовима ХПВ-а. Природни флороглуцинолски деривати из *Rhodomyrtus tomentosa* показали су потенцијал против карцинома грлића материце, али њихови механизми повезани са апоптозом и даље су недовољно разјашњени. У овом раду, одабрани флороглуцинолски деривати процењени су као потенцијални инхибитори анти-апоптотског протеина Bcl-2 (PDB: 6GL8) применом интегрисаног *in silico* приступа који обухвата молекулски докинг, 100 ns молекулску динамику, MM/GBSA процену слободне енергије везивања, ADMET профилисање и DFT анализу електронских својстава. Докинг резултати су издвојили CPD1 као најповољнији лиганд (-37,36 kJ/mol), бољи од белзутифана (-25,73 kJ/mol), уз стабилно уклапање у конзервирани везујући џеп. Трајекторије MD симулација

подржале су стабилно формирање комплекса током 100 ns. MM/GBSA анализа додатно је указала на јаче везивање CPD1 (ΔTOTAL = -138,78 ± 15,4 kJ/mol) у односу на белзутифан (-63,72 ± 14,31 kJ/mol), пре свега услед повољнијих интеракција у гасној фази, уз задржавање упоредивог солватационог доприноса. ADMET предвиђања указала су на сличну растворљивост, али и већу интестиналну апсорпцију CPD1, као и присуство hERG II сигнала који захтева даљу оптимизацију у контексту кардиотоксичности. Добијени DFT дескриптори су у складу са појачаним електрофилним карактером CPD1. У целини, CPD1 је рачунарски идентификован као приоритетни скелет за даљу експерименталну валидацију и структурално вођену оптимизацију.

(Примљено 13. децембра 2025; ревидирано 26. фебруара 2026; прихваћено 23. марта 2026.)

REFERENCES

1. F. Bray, M. Laversanne, H. Sung, J. Ferlay, R. L. Siegel, I. Soerjomataram, A. Jemal, *CA. Cancer J. Clin.* **74** (2024) 229 (https://doi.org/10.3322/caac.21834)
2. K. S. Okunade, *J. Obstet. Gynaecol.* **40** (2020) 602 (https://doi.org/10.1080/01443615.2019.1634030)
3. M. Bida, B. Mosoane, B. Phakathi, M. Sebitloane, M. Z. Muallem, R. Hull, Z. Dlamini, in *Cancer Sensitizing Agents for Chemotherapy*, Z. Dlamini, Ed., Academic Press, Oxford, 2024, p. 17 (https://doi.org/10.1016/B978-0-443-28985-9.00005-7)
4. S. Ashique, M. Bhowmick, R. Pal, H. Khatoon, P. Kumar, H. Sharma, A. Garg, S. Kumar, U. Das, *Adv. Cancer Biol. - Metastasis* **10** (2024) 100114 (https://doi.org/10.1016/j.adcanc.2024.100114)
5. P. Ray, D. Paul, *Pharmacol. Res. - Mod. Chinese Med.* **12** (2024) 100497 (https://doi.org/10.1016/j.prmcm.2024.100497)
6. F. Qi, L. Zhao, A. Zhou, B. Zhang, A. Li, Z. Wang, J. Han, *Biosci. Trends* **9** (2015) 16 (https://doi.org/10.5582/bst.2015.01019)
7. Y. Zhou, J. Zheng, Y. Li, D. P. Xu, S. Li, Y. M. Chen, H. B. Li, *Nutrients* **8** (2016) 515 (https://doi.org/10.3390/nu8080515)
8. M. H. Kang, I. H. Kim, T. J. Nam, *Int. J. Oncol.* **45** (2014) 1036 (https://doi.org/10.3892/ijo.2014.2521)
9. Y. Peng, Y. Wang, C. Zhou, W. Mei, C. Zeng, *Front. Oncol.* **12** (2022) 819128 (https://doi.org/10.3389/fonc.2022.819128)
10. E. C. Aniogo, B. P. George, H. Abrahamse, *Molecules* **25** (2020) 5308 (https://doi.org/10.3390/molecules25225308)
11. N. V. Pervushin, G. S. Kopeina, B. Zhivotovsky, *Biol. Direct* **18** (2023) 69 (https://doi.org/10.1186/s13062-023-00431-4)
12. T. I. Adelusi, A. Q. K. Oyedele, I. D. Boyenle, A. T. Ogunlana, R. O. Adeyemi, C. D. Ukachi, M. O. Idris, O. T. Olaoba, I. O. Adedotun, O. E. Kolawole, Y. Xiaoxing, M. Abdul-Hammed, *Informatics Med. Unlocked* **29** (2022) 100880 (https://doi.org/10.1016/j.imu.2022.100880)
13. D. Jeong, W. S. Yang, Y. Yang, G. Nam, J. H. Kim, D. H. Yoon, H. J. Noh, S. Lee, T. W. Kim, G. H. Sung, J. Y. Cho, *J. Ethnopharmacol.* **146** (2013) 205 (https://doi.org/10.1016/j.jep.2012.12.034)
14. Y. B. Zhang, W. Li, L. Jiang, L. Yang, N. H. Chen, Z. N. Wu, Y. L. Li, G. C. Wang, *Phytochemistry* **153** (2018) 111 (https://doi.org/10.1016/j.phytochem.2018.05.018)

15. J. B. Murray, J. Davidson, I. Chen, B. Davis, P. Dokurno, C. J. Graham, R. Harris, A. Jordan, N. Matassova, C. Pedder, S. Ray, S. D. Roughley, J. Smith, C. Walmsley, Y. Wang, N. Whitehead, D. S. Williamson, P. Casara, T. Le Diguarher, J. Hickman, J. Stark, A. Kotschy, O. Geneste, R. E. Hubbard, *ACS Omega* **4** (2019) 8892 (https://doi.org/10.1021/acsomega.9b00611)

16. G. M. Morris, R. Huey, W. Lindstrom, M. F. Sanner, R. K. Belew, D. S. Goodsell, A. J. Olson, *J. Comput. Chem.* **30** (2009) 2785 (https://doi.org/10.1002/jcc.21256)

17. H. D. Nguyen, *Not. Sci. Biol.* **17** (2025) 12642 (https://doi.org/10.55779/nsb17312642)

18. D. Van Der Spoel, E. Lindahl, B. Hess, G. Groenhof, A. E. Mark, H. J. C. Berendsen, *J. Comput. Chem.* **26** (2005) 1701 (https://doi.org/10.1002/jcc.20291)

19. N. Guex, M. C. Peitsch, *Electrophoresis* **18** (1997) 2714 (https://doi.org/10.1002/elps.1150181505)

20. V. Zoete, M. A. Cuendet, A. Grosdidier, O. Michielin, *J. Comput. Chem.* **32** (2011) 2359 (https://doi.org/10.1002/jcc.21816)

21. H. D. Nguyen, *Indian J. Chem.* **64** (2025) 383 (https://doi.org/10.56042/ijc.v64i4.15530)

22. M. S. Valdés-Tresanco, M. E. Valdés-Tresanco, P. A. Valiente, E. Moreno, *J. Chem. Theory Comput.* **17** (2021) 6281 (https://doi.org/10.1021/acs.jctc.1c00645)

23. D. E. Pires, T. L. Blundell, D. B. Ascher, *J. Med. Chem.* **58** (2015) 4066 (https://doi.org/10.1021/acs.jmedchem.5b00104)

24. F. Neese, *WIREs Comput. Mol. Sci.* **15** (2025) e70019 (https://doi.org/10.1002/wcms.70019)

25. G. Knizia, J. E. Klein, *Angew. Chemie Int. Ed.* **54** (2015) 5518 (https://doi.org/10.1002/anie.201410637)

26. M. D. Hanwell, D. E. Curtis, D. C. Lonie, T. Vandermeersch, E. Zurek, G. R. Hutchison, *J. Cheminform.* **4** (2012) 17 (https://doi.org/10.1186/1758-2946-4-17)

27. J. Luo, Z. Q. Xue, W. M. Liu, J. L. Wu, Z. Q. Yang, *J. Phys. Chem. A* **110** (2006) 12005 (https://doi.org/10.1021/jp063669m)

28. R. Das, J. L. Vigneresse, P. K. Chattaraj, *Int. J. Quantum Chem.* **114** (2014) 1421 (https://doi.org/10.1002/qua.24706)

29. P. C. Agu, C. A. Afiukwa, O. U. Orji, E. M. Ezeh, I. H. Ofoke, C. O. Ogbu, E. I. Ugwuja, P. M. Aja, *Sci. Rep.* **13** (2023) 13398 (https://doi.org/10.1038/s41598-023-40160-2)

30. D. A. Schaller, C. D. Christ, J. D. Chodera, A. Volkamer, *J. Chem. Inf. Model.* **64** (2024) 8848 (https://doi.org/10.1021/acs.jcim.4c00905)

31. R. Patil, S. Das, A. Stanley, L. Yadav, A. Sudhakar, A. K. Varma, *PLoS One* **5** (2010) e12029 (https://doi.org/10.1371/journal.pone.0012029)

32. G. Bitencourt-Ferreira, M. Veit-Acosta, W. F. de Azevedo, in *Docking Screens for Drug Discovery*, W. F. de Azevedo Jr., Ed., Springer, New York, 2019, p. 79 (https://doi.org/10.1007/978-1-4939-9752-7_6)

33. H. Alonso, A. A. Bliznyuk, J. E. Gready, *Med. Res. Rev.* **26** (2006) 531 (https://doi.org/10.1002/med.20067)

34. L. Martínez, *PLoS One* **10** (2015) e0119264 (https://doi.org/10.1371/journal.pone.0119264)

35. M. L. Verteramo, M. M. Ignjatović, R. Kumar, S. Wernersson, V. Ekberg, J. Wallerstein, G. Carlström, V. Chadimová, H. Leffler, F. Zetterberg, D. T. Logan, U.

Ryde, M. Akke, U. J. Nilsson, *iScience* **27** (2024) 109636 (https://doi.org/10.1016/j.isci.2024.109636)

36. H. D. Nguyen, *Phys. Chem. Res.* **13** (2025) 783 (https://doi.org/10.22036/pcr.2025.535946.2708)

37. H. Rohit, H. Tandon, *J. Mol. Model.* **31** (2025) 291 (https://doi.org/10.1007/s00894-025-06487-5)

38. B. Bashir, A. Z. Clayborne, *Molecules* **30** (2025) 2254 (https://doi.org/10.3390/molecules30112254).